COMPUTED TWO-PHASE RELATIVE PERMEABILITY USING DIGITAL ROCK PHYSICS IN A SHALE FORMATION

Michael Suhrer, Jonas Toelke[2], Michael Suhrer[2], Elizabeth Diaz[2], Avrami Grader[2], Joel Walls[2], Dora P. Restrepo[1], Maria T. Cantisano[1], Sandra Cespedes[1]

[1]Ecopetrol, Bogota, Colombia
[2]Ingrain Inc., Houston, USA

This paper was prepared for presentation at the International Symposium of the Society of Core Analysts held in Napa Valley, California, USA, 16th to 19th September 2013

ABSTRACT

Simultaneous flow of two liquid phases through an organic shale pore system was modeled using a Lattice-Boltzmann method. This paper describes the methods and results of this modeling project which was designed to quantify the range of expected permeability and relative permeability in samples from a shale formation in Colombia. Porosity versus absolute permeability trends were determined for 44 well samples using digital rock physics (DRP) methods. The formation samples average about 6% organic material content by volume. The total porosity range observed is from about 3 to 15%. For total porosity of 4% or above, the calculated horizontal permeability is generally above 100 nano-Darcy (nD). For porosity of 8%, the calculated horizontal permeability is typically 1000 nD or more. From these 44 samples, four were selected for oil-water and two for gas-water relative permeability analysis. Two phase flow modeling was conducted using several scenarios. Imbibition relative permeability computations with increasing fractional flow ratios of water were performed for oil-water systems for different scenarios including different contact angles ranging from oil to water wet, and for different API values resulting in different viscosity ratios. Gas-water relative permeability computations were performed for increasing fractions of gas.

INTRODUCTION

Historically, shales were thought to perform two key functions, act as a seal for conventional reservoirs and as a source rock for hydrocarbons. Recently, several shale formations have also proven to be major self-sourcing hydrocarbon reservoirs. The establishment of liquids production from numerous shale plays confirmed shale as an important source of hydrocarbons and spurred a worldwide assessment of shale production potential. Although the Gas Research Institute (GRI) process using crushed samples (1) allows a relatively quick measurements of both porosity and permeability, the assessment of relative permeabilities is not possible. Here recent improvements in SEM sample preparation, selection and imaging (2) and the use of pore scale flow simulators (3) make it possible to compute meaningful relative permeability curves for shale rock. This paper describes the methodology and results of an unconventional reservoir study to assess relative permeability functions and their sensitivities with respect to wetting properties and viscosity ratios.

METHODS

Low Electron Beam Energy SEM Imaging:

High-resolution, dual energy CT imaging of the whole core, with computed bulk density and photo-electric factor, were used to quality control potential sample locations and to orient plugs taken from the preserved core. Whole core dual-energy CT imaging produces image voxel dimensions of about 0.5mm. The plugs were then Micro-CT imaged (20 to 40 micron voxel dimensions) to locate representative areas within the plug for ion milling. A working area about 1 mm^2 was milled with an argon ion mill. A swath of about ten 2D images was captured at approximately 10 nm per pixel using both secondary electron (SE2) and back-scatter electron (BSE1) detectors. The SE2 images were used primarily to locate porosity and pore boundaries, which are important for segmentation, while BSE1 images were helpful in discerning mineralogical variations, organic matter, and grain/crystal boundaries. The 2D SEM images were segmented for matrix minerals, heavy minerals, organic matter, and porosity using a combination of Ingrain Inc. proprietary algorithms and commercial visualization software. These interpretations provided information about mineralogical distribution, porosity types, and organic matter textures. The 2D SEM images were used to select areas of interest for 3D FIB-SEM imaging. Local porosity theory was used to assess the characteristic features of the pore space, heterogeneities, anisotropic behavior and estimate a length scale for the representative elementary volume (REV) (4; 5).

The areas identified for 3D imaging were mounted and inserted into a FIB-SEM imaging system. The 3D image data sets were acquired by alternately removing about 10 nm of material with the Ga+ ion beam from a prepared area, and acquiring SE2 and BSE1 images. This process of milling and imaging parallel surfaces is repeated around 600 to 1,000 times. After capturing all of the individual FIB-SEM images, they were aligned and merged into separate SE2 and BSE1 3D objects with each image voxel having dimensions of from 10 to 15 nanometers. The FIB-SEM process used in this paper is described in (6).

The 3D volume is then segmented using Ingrain Inc. proprietary 3D algorithms that separate pore space, porosity associated with organic matter, solid organic matter, and solid matrix framework into separate 3D volumes. Finally, the digital pore volume object is used in numerical computations. It is important to note that the data used to illuminate shale microstructure in the FIB-SEM 3D volumes represents a very small amount of rock; typically about 2×10^{-9} g as compared with around 300 g of material used for the GRI process in measuring porosity and permeability.

Pore size and pore throat size distribution:

The hydraulic pore size distribution is based on the opening map of the pore space. In the opening map every pore voxel has as value the radius of the largest sphere that can be inscribed in the pore space without intersecting a solid voxel. It describes the openness of the pore space. Low values of the opening map indicate that the corresponding voxel belongs to small features of the pore space, large values that the voxel belongs to a large feature. Separating the voxels at a certain threshold r_t of the opening map can be seen as an approximation of the spatial distribution of the wetting (small values in the opening

map) and non-wetting (large values in the opening map) phase at the capillary pressure $2 \sigma \cos \theta / r_t$ for a perfectly wetting situation. Building the cumulative values of the pore volume occupied by the values larger than a certain value in the opening map gives a cumulative pore size distribution. The pore throat size distribution can be computed by a Digital equivalent of the mercury injection capillary pressure. This is achieved by increasing the digital pressure step by step and adding connectivity to the opening map, meaning that the invading phase (e.g.: mercury in the real world) has to have a connection to invade the sample (7; 8).

Relative permeability computation for shale rocks:

In general, pore-scale immiscible flow of two phases is described by the Stokes equations, separate for each fluid and an interface condition at the moving fluid-fluid interface, including the capillary pressure. The pressure difference between the two fluids at the interface depends on the interfacial tension and the two principal radii of curvature of the interface surface. Another important ingredient of a two-phase flow simulation in porous media is the contact angle at the fluid/fluid/solid (triple lines) boundary. The dimensionless parameters that impact two phase Stokes flow are the capillary number and the viscosity ratio of the fluids. In a capillary dominated flow regime the distribution of the fluid phases inside the rock are determined by the initial conditions, the wettability and the fractional flow ratios. The effect of viscosity ratio on relative permeability curves has provoked a continuing discussion (9). In general, a strong effect of the viscosity ratio on the relative permeability curves is not observed experimentally in sandstones and carbonates (e.g.: discussion in (10)). An argument for this is that the two fluids occupy distinct pore networks inside the rocks and the viscous coupling between the two fluids does not play a role. There are some artificial testcases where viscous coupling has an effect on relative permeabilities (11; 12). We include the viscosity ratio in our parameter study, since the structure of the pore network of shales is different from sandstone and carbonates.

A uniform wettability is given for most gas-liquid systems, but for liquid-liquid systems it is related to a clean, mono-crystalline solid surface. Reservoir rocks often have different minerals covering the surface, with different water repelling or attracting properties. Also the saturation history (the aging process) has an important effect on wettability. Shales are different from sandstones and carbonates in many ways and wettability is a complex issue for digital rock physics since a wettability distribution has to be assigned to the rock surface (14). A scenario for shales might be that the surface of organic matter pores is oil wet whereas the pores enclosed by minerals are more water-wet. The presence of clays complicates this situation even more (15). Modeling of wettability in shales has been presented in (16). In this study we used two limiting cases for the oil-water system: a uniformly oil-wet and water-wet case. The authors acknowledge that this is not the reality, but that it helps to judge the variability of the relative permeability with respect to the wetting conditions. The initial conditions, the distribution of the oil and water in the beginning, are also an unknown in the simulation of the relative permeability of shale rock. In a ‘conventional’ SCAL analysis (either physical or digital) a primary drainage is performed up to a certain pressure and the rock

is aged. This state is the initial condition for the imbibition simulation. For a shale rock we do not have a procedure like this and it is even not appropriate due to the conversion process of the organic matter. It is expected that organic matter pores contain oil. A possible way to obtain more realistic initial conditions is probably to use information form well-logs and to distribute the liquids in a reasonable way. In this study we use for simplicity a fully saturated rock and the authors are aware that this is a severe simplification.

In shales pore throats can be in the order of a few nanometers. Here the assumption of continuous flow regime may be not very accurate for gas flow and slip effects due to finite Knudsen numbers may increase gas permeability. An opposite effect has the adsorbed layer of gas at the throats that depends on the in-situ pressure conditions and the throat sizes. This leads to a complex functional dependence and the gas permeability can be larger or smaller than the liquid permeability depending on the reservoir pressure and the pore throat size (13). We compute in all cases base liquid permeability even when gas flow is involved. Relations developed in (13) can then be used to adapt gas permeabilities to in-situ conditions.

The numerical solution of the Partial Differential Equations (PDEs) describing two-phase displacement in the pore scale is an extremely demanding task due to complex physics with moving interfaces in a highly complex pore geometry, the implementation of the contact angle at the triple lines, time dependent boundary conditions, the use of feedback methods and a huge number of degrees of freedom. The lattice Boltzmann method (LBM) is an efficient numerical scheme for the simulation of fluid flow. The fundamental idea of this method is to construct simplified kinetic models that incorporate the physics of microscopic and/or mesoscopic phenomena in a way that the macroscopic-averaged properties obey the desired continuum equations (17). In a two-phase implementation of LBM, a second field (besides the flow field) is introduced representing the distribution of the phases and the computations are extended to include the interfacial forces (18). The simulations are run on high performance computing (HPC) hardware to cope with the enormous computational load (19; 20).

For oil-water relative permeabilities we use a fractional flow approach as described in (3). We start the simulation with a fully oil saturated rock and increase step by step the fraction of water flowing until a quasi-stationary state is reached. By computing the saturation and pressure profiles from the field solution we can construct relative permeability curves. For gas-water and gas-oil relative permeabilities where gas comes out of solution for declining pressure the gas is placed digitally in the largest pore space using information from the opening map. At the beginning oil or water permeability is reduced, but gas is not connected and can't flow. At a certain saturation, the critical gas saturation, gas phase becomes connected and starts to flow. From this point on the relative permeability is computed by the fractional flow approach.

Results for the Columbian shale formation:

We selected 6 out of the 44 3D samples and determined connected and isolated porosity, organic volume fraction, pore body and pore throat size distribution, absolute permeability in horizontal direction (see Table 1) and finally relative permeability.

Samples B, A, F and G were selected for oil-water and samples W1 and W2 were selected for gas-water relative permeability analysis.
Figure 1 shows the digitized rocks used for the simulations, black is pore space, darker gray is organic matter and lighter gray are minerals. Figure 2 shows the pore size and pore throat size distribution of the samples. For samples B, A and F the throat size at 50% invaded volume is between 33 and 44 nanometer, whereas the pore size ranges between 110 and 120 nanometer. Sample G is considerably larger with throats around 70 nanometer and pores around 200 nanometer and samples W1 and W2 are smaller with throats around 20 nanometers and pores around 60 nanometers. Table 1 shows the ratio between pores and throats and it is around 3 for 50% of invaded pore space in all cases.
Imbibition relative permeability runs (increasing fractional flow of water) were performed for oil-water systems for different scenarios including different contact angles ranging from oil to water wet and different API values leading to different viscosity ratios. Table 2 summarizes the different scenarios from oil- to water wet and different scenarios for petro-physical properties like API, GOR and bubble point pressure leading to different oil viscosities and therefore to different viscosity ratios of the fluid-fluid systems. Figure 4 shows snapshots of the fluid distributions, oil: blue and water: green in the pore system for the oil wet case 1 for increasing fractional flows of water in sample A. Figure 5 to Figure 8 show the relative permeability curves for the different scenarios for samples B, A, F and G. Gas-water relative permeability runs were performed for increasing fractional flow of gas and are shown in Figure 9.

OBSERVATIONS AND CONCLUSIONS

Digital Rock Physics analysis brings several advantages to the process of shale reservoir characterization: It can distinguish between multiple porosity types (connected, isolated, and porosity associated with organic material), it can give an estimation of TOC, permeability in horizontal and vertical directions, it can compute the pore body and pore throat sizes and compute relative permeability curves using different scenarios based on simplifying modeling assumptions.

For the simulated oil-water relative permeabilities we see the following trends:
Wettability: The scenarios water-wet (54°) and oil-wet (135°) have a substantial impact of the shape and end points of the relative perm curves. The crossing is consistent for all cases and is below S_w=0.5 for oil-wet cases and above for water wet cases. Also $k_{ro\_ww} > k_{ro\_ow}$ and $k_{rw\_ow} > k_{rw\_ww}$ for the same saturation value consistently. Also $k_{rw\_ow}(S_w=1-S_{or\_ow})$ is larger than 0.5. Unusual are the values for S_{or} for the water-wet cases. In all cases $S_{or\_ow} > S_{or\_ww}$, which is not observed usually. This leads also to the unusual fact that $k_{rw\_ww}(S_w=1-S_{or\_ww}) > k_{rw\_ow}(S_w=1-S_{or\_ow})$ for sample B and G. The imbibition in the water wet case of a 100% oil saturated medium might be responsible for this effect (behaving more like a piston-like displacement) and more realistic initial conditions might give different results.

Viscosity ratio: Different viscosity ratios lead to far less variation in the curves than the variation due to the change in wettability. Nevertheless a consistent trend for the oil-wet and water-wet cases can be observed: For a higher viscosity ratio defined as $vr=\mu_{oil(or\ gas)}/\mu_w$ we get a lower k_{rw} and a higher k_{ro}. The viscosity ratio variation in all cases is going from below 1 to above 1. This is consistent with the observations in (12) for a sintered Teflon medium. Nevertheless this is an unusual result and is not observed for experimental results in sandstone and carbonate rocks. One explanation might be that in shale rock water and oil share larger interface that could enhance viscous coupling effects. Another explanation especially for the water wet case might be capillary micro-fingering (21). Although in a capillary dominated regime overall viscous forces are small, there can be strongly localized effects leading to a difference in the distribution of liquids. In Figure 3 the distribution of oil(light blue) and water(red) in a slice perpendicular to the flow direction is shown for sample G, the two water-wet cases at S_w=0.45. There are slight differences in distribution of liquids that have a measurable effect on the relative permeability as shown in Figure 8. Overall the results for the oil-water relative permeability curves show some unusual features and need further investigation. Especially the cases with high API values lead to oil viscosities lower than the water viscosities and this indicates very good displacement efficiency.

The gas-water relative permeabilities show a critical gas saturation of 0.14 and a S_{rw} of 30% for sample W1 and a critical gas saturation of 0.18 and a S_{rw} of 40% for sample W2.

Outlook: In the future we want to take mixed wettability into account, where organic matter surface is treated as oil wet, and the mineral surfaces as water wet. Also we want to take information from well logs into account to model more realistic initial conditions. It would be helpful at some point to have experimental proof though flow experiments, but this a very difficult task to achive for multiphase flow in shales.

ACKNOWLEDGEMENT

The authors would like to thank Ecopetrol of Bogota, Colombia for permission to present these results.

REFERENCES

1. **Guidry, K., Luffel, D. and Curtis, J.** *Development of laboratory and petrophysical techniques for evaluating shale reservoirs—final technical report.* Gas Research Institute. 1995. p. 286. Report GRI-95/0496.
2. **Driskill, B., et al.** Applications of SEM Imaging to Reservoir Characterization in the Eagle Ford Shale, South Texas, USA. [book auth.] W. K. Camp, E. Diaz and B. Wawak. *Electron Microscopy of Shale Hydrocarbon Reservoirs.* 2013. AAPG Memoir 102.
3. *Computation of relative permeability functions in 3D digital rocks by a fractional flow approach using the lattice Boltzmann method.* **De Prisco, G, Toelke, J and Dernaika, M.R.** 2012. SCA2012-36.

4. *Process Based Reconstruction of Sandstones and Prediction of Transport Properties.* **Oren, P. and Bakke, S.** 2002, Transport in Porous Media, Vol. 46, pp. 311–343.
5. *Three-dimensional local porosity analysis of porous media.* **Biswal, B., Manwarth, C. and Hilfer, R.** 1998, Physica A, Vol. 255, pp. 221-241.
6. **Huang, J., Cavanaugh, T. and Nur, B.** An introduction to SEM operational principles and geologic applications for shale hydrocarbon reservoirs. [book auth.] W. K. Camp, E. Diaz and B. Wawak. *Electron microscopy of shale hydrocarbon reservoirs.* 2013. AAPG Memoir 102.
7. *Simulation of capillary-dominated displacements in micro-tomographic images of reservoir rocks.* **Hazlett, R. D.** 1995, Transport in Porous Media, Vol. 20, pp. 21-35.
8. *Pore-morphology-based simulation of drainage in totally wetting porous media.* **Hilpert, M. and Miller, C. T.** 2001, Advances in Water Resources, Vol. 24, pp. 243-255.
9. **Honarpour, M. M., Koederitz, F. and Herbert, A.** *Relative permeability of petroleum reservoirs.* 1986.
10. **Dullien, F. A.** *Porous media: fluid transport and pore structure.* 1991.
11. **Odeh, A. S.** *Effect of viscosity ratio on relative permeability.* 1958. PHD thesis.
12. *Factors affecting liquid-liquid relative permeabilities of a consolidated porous medium.* **Lefebvre du, P. R. E. Y.** 1, 1973, Old SPE Journal, Vol. 13, pp. 39-47.
13. *Gas Permeability of Shale.* **Sakhaee-Pour, A. and Bryant, S. L.** 2011. SPE Annual Technical Conference and Exhibition, 30 October-2 November 2011, Denver, Colorado, USA.
14. *NMR Study of Shale Wettability.* **Odusina, E., Sondergeld, C. and Rai, C.** 2011. Canadian Unconventional Resources Conference.
15. *Experimental investigations of the wettability of clays and shales.* **Borysenko, A., et al.** B7, 2009, Journal of Geophysical Research: Solid Earth, Vol. 114, pp. 2156-2202.
16. *Wettability estimation of low-permeability, siliceous shale using surface forces.* **Takahashi, S. and Kovscek, A. R.** 1, 2010, Journal of Petroleum Science and Engineering, Vol. 75, pp. 33-43.
17. *Lattice gas hydrodynamics in two and three dimensions.* **Frisch, U., et al.** 1987, Complex Systems, Vol. 1, pp. 75–136.
18. *A lattice Boltzmann method for immiscible two-phase Stokes flow with a local collision operator.* **Toelke, J., De Prisco, G. and Mu, Y.** 6, 2013, Computers and Mathematics with Applications, Vol. 65, pp. 864–881.
19. *TeraFLOP Computing on a Desktop PC with GPUs for 3D CFD.* **Toelke, J. and Krafczyk, M.** 7, 2008, International Journal of Computational Fluid Dynamics, Vol. 22, pp. 443-456.
20. **Toelke, J.** *Lattice Boltzmann Multi-Phase Simulations in Porous Media using GPUs.* 2010. GTC2010, http://nvidia.fullviewmedia.com/gtc2010/0922-e-2170.html.
21. *On the role of the viscosity ratio during low-capillary-number forced imbibition in porous media.* **Vizika, O., Avraam, D. G. and Payatakes, A. C.** 2 , 1994, Journal of colloid and interface science, Vol. 165, pp. 386-401.

Table 1: Porosity, permeability and ratios of pore body to pore throat size at a cumulative Saturation of 0.5.

	B	A	F	G	W1	W2
Porosity [%]	**11.7**	**14.3**	**10.1**	**11.6**	**8.3**	**6.5**
Permeability [nD]	**3100**	**3900**	**2100**	**12000**	**800**	**300**
Ratio Pore to Throat	**3.3**	**2.7**	**2.9**	**3.1**	**2.6**	**2.6**

Table 2: Different scenarios for the sensitivity study.

sample	**A (oil)**			**B (oil)**			**G (oil)**			**F (oil)**		**W2 (gas)**	**W1 (gas)**
API	25	38	38	25	38	38	33	42	33	31	42	61	61
Contact Angle (o)	135	135	54	135	54	135	135	54	54	135	54	20	20
Viscosity Water (cp)	0.48	0.43	0.43	0.48	0.43	0.43	0.37	0.29	0.29	0.37	0.29	0.37	0.21
Viscosity Oil(Gas) (cp)	1.27	0.22	0.22	1.27	0.22	0.22	0.36	0.22	0.52	0.58	0.18	0.037	0.034
Viscosity ratio Oil(Gas)/Water	2.6	0.51	0.51	2.6	0.51	0.51	0.97	0.76	1.8	1.6	0.62	0.10	0.16

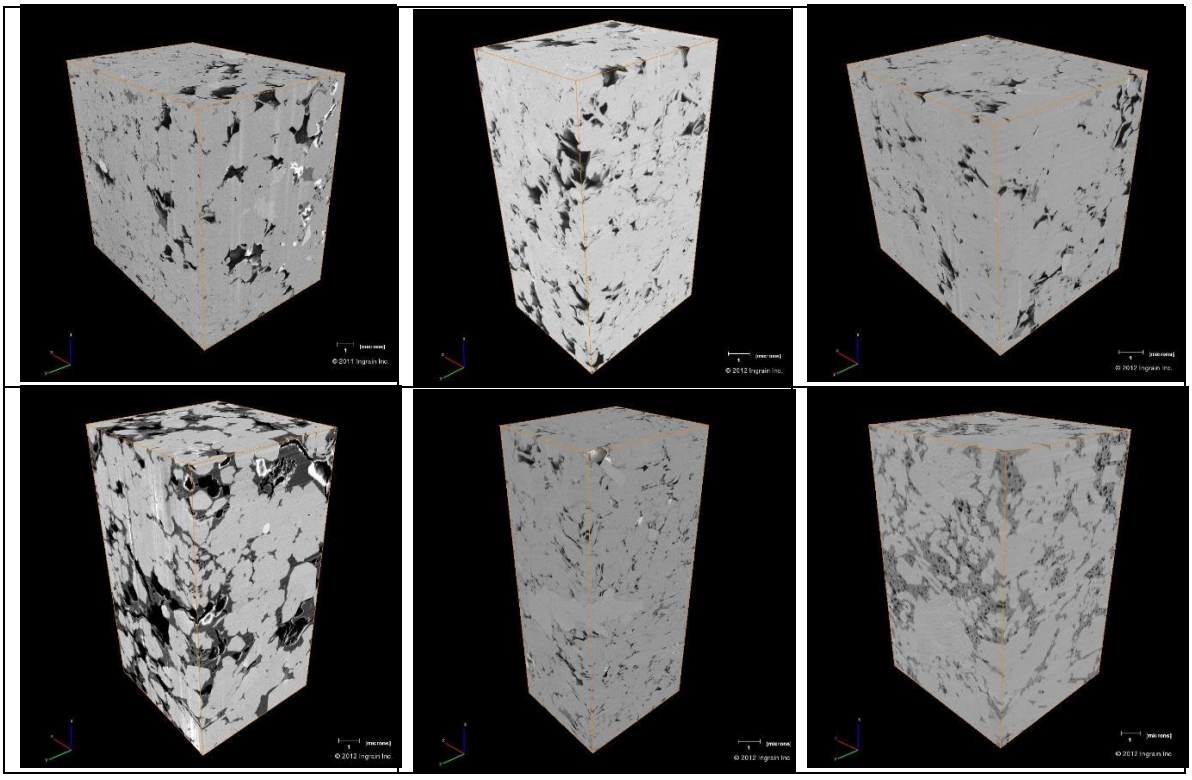

Figure 1: Digital rock samples B, A, F, G, W1, W2 (from left to right and top to bottom) for relative permeability computations. B, A, F, G are oil-water and W1,W2 are gas-water cases.

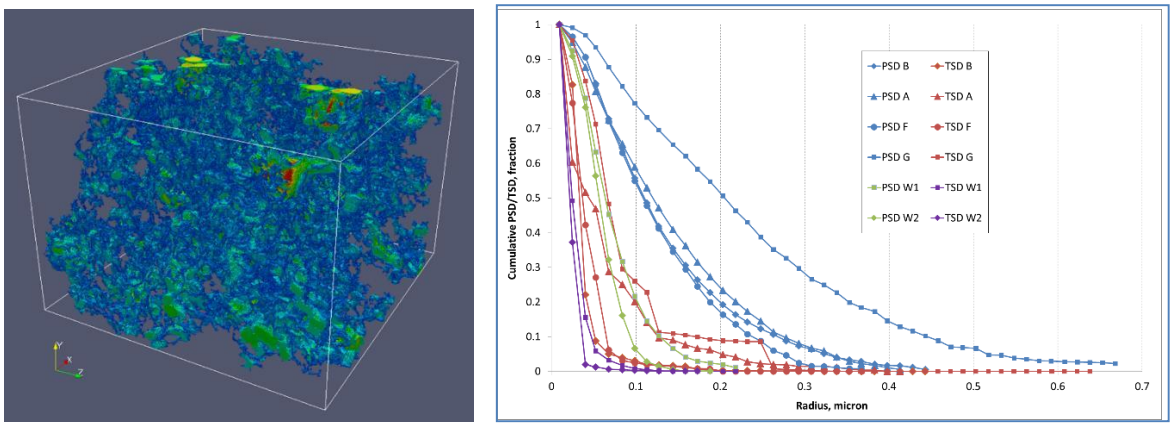

Figure 2: Left: Opening map of sample B, Right: pore body size versus pore-throat size for samples B, A, F, G.

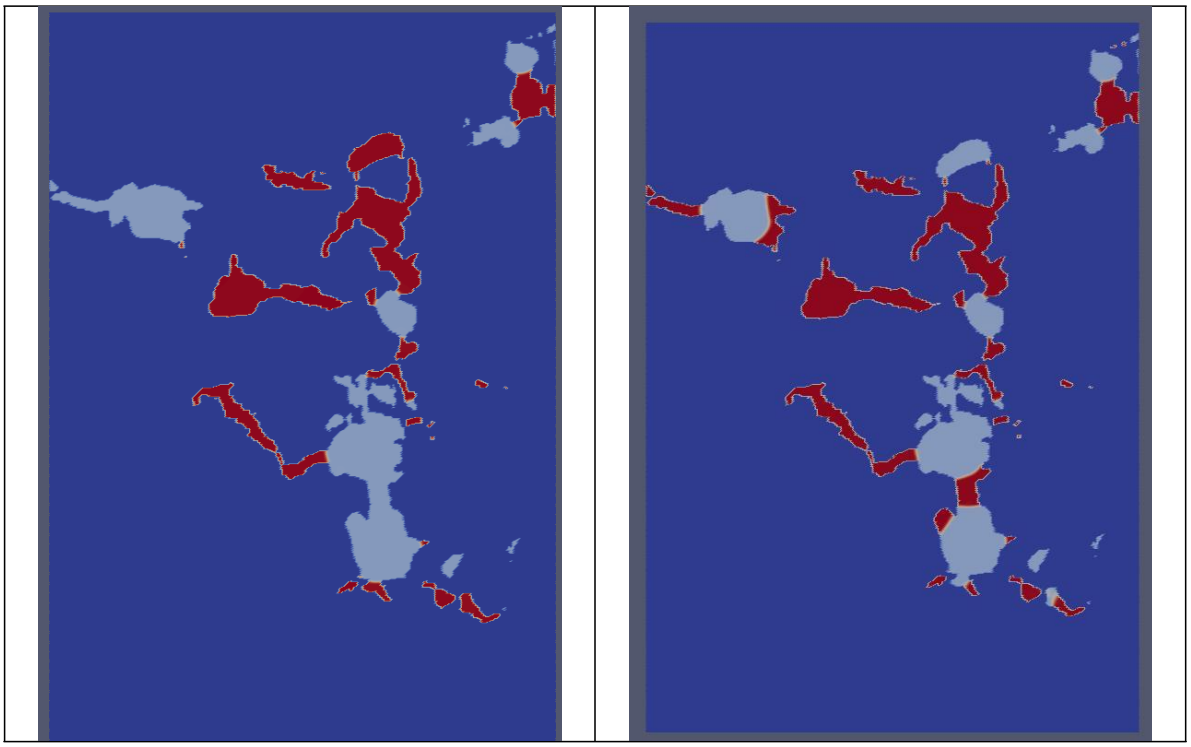

Figure 3: Left: Sample G, water-wet, API 33, Sw=0.45, Right: Sample G, water-wet, API 42, Sw=0.45. water(red), oil(light blue), matrix(dark blue).

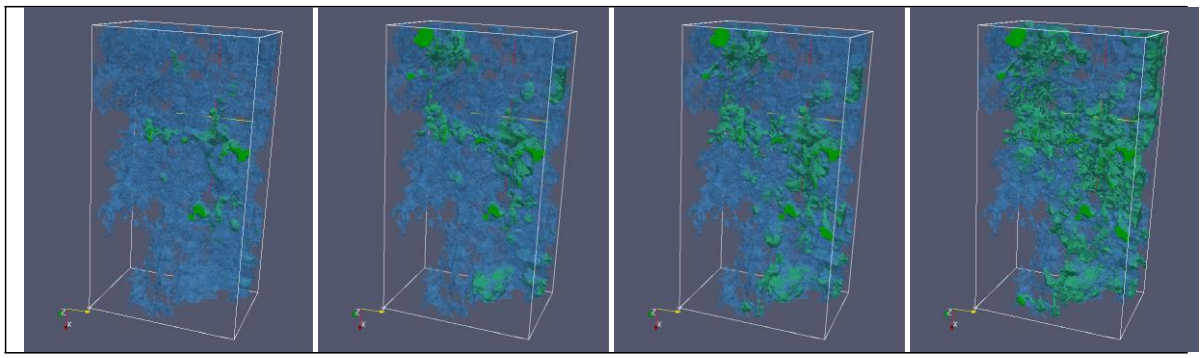

Figure 4: Distribution of oil (blue) and water (green) for different (increasing) fractional flow ratios of water in sample A, oil wet case.

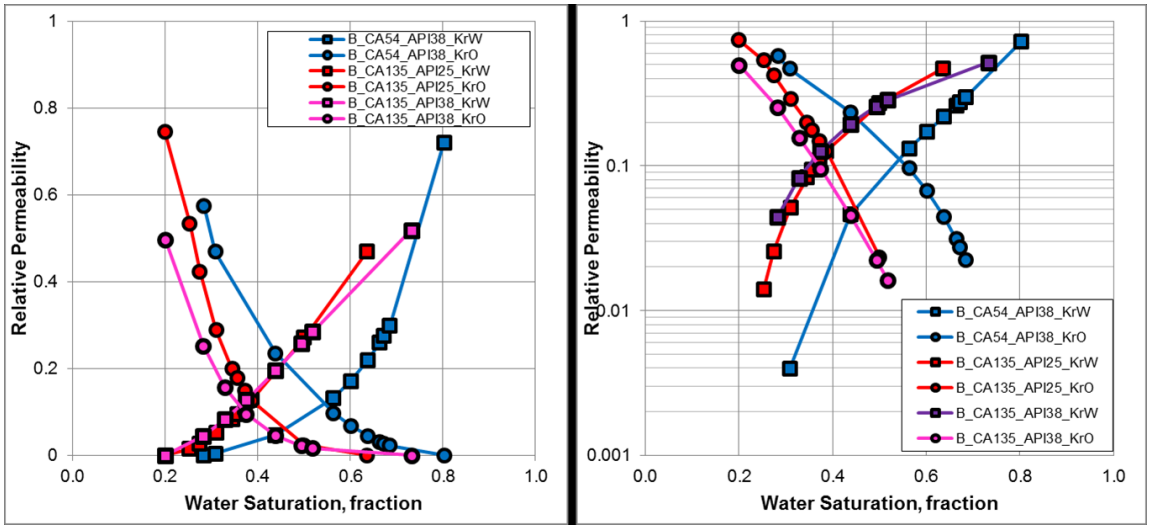

Figure 5: Relative permeability for sample B. Oil-wet case 1 (red curves, contact angle 135^0, API 25), oil-wet case 2 (pink curves, contact angle 135^0, API 38), and water-wet case (bluw curves, contact angle 54^0, API 38).

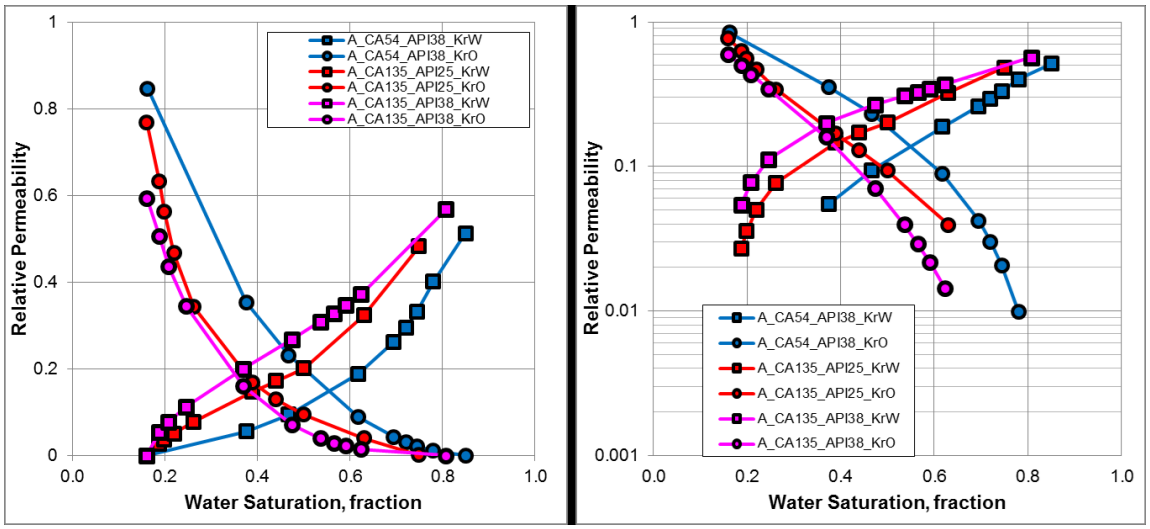

Figure 6: Relative permeability for sample A. Oil-wet case 1 (red curves, contact angle 135^0, API 25), oil-wet case 2 (pink curves, contact angle 135^0, API 38), and water-wet case (blue curves, contact angle 54^0, API 38)

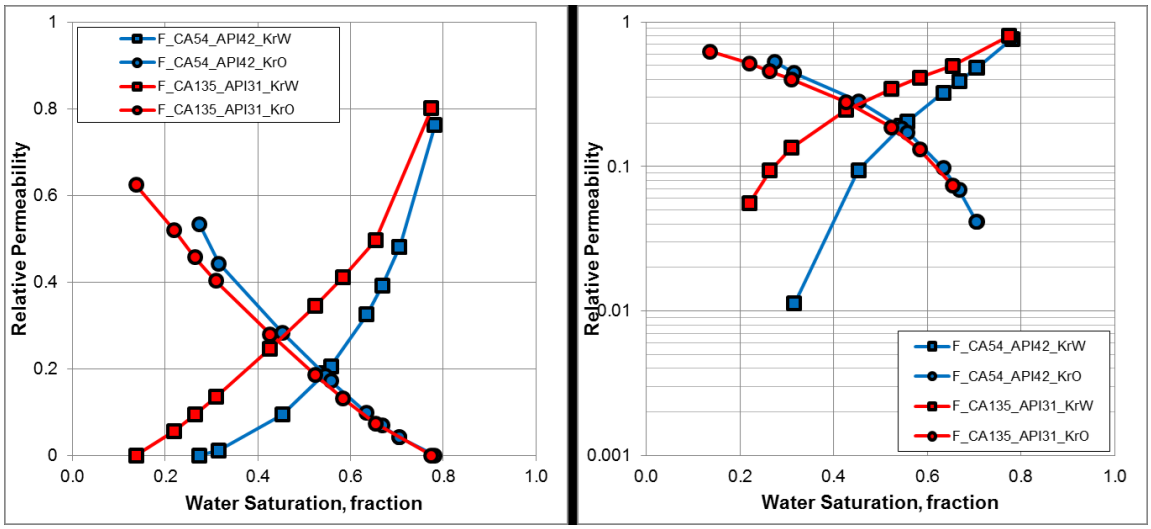

Figure 7: Relative permeability for sample F. Oil-wet case (red curves, contact angle 135^0, API 31) and water-wet case (blue curves, contact angle 54^0, API 42)

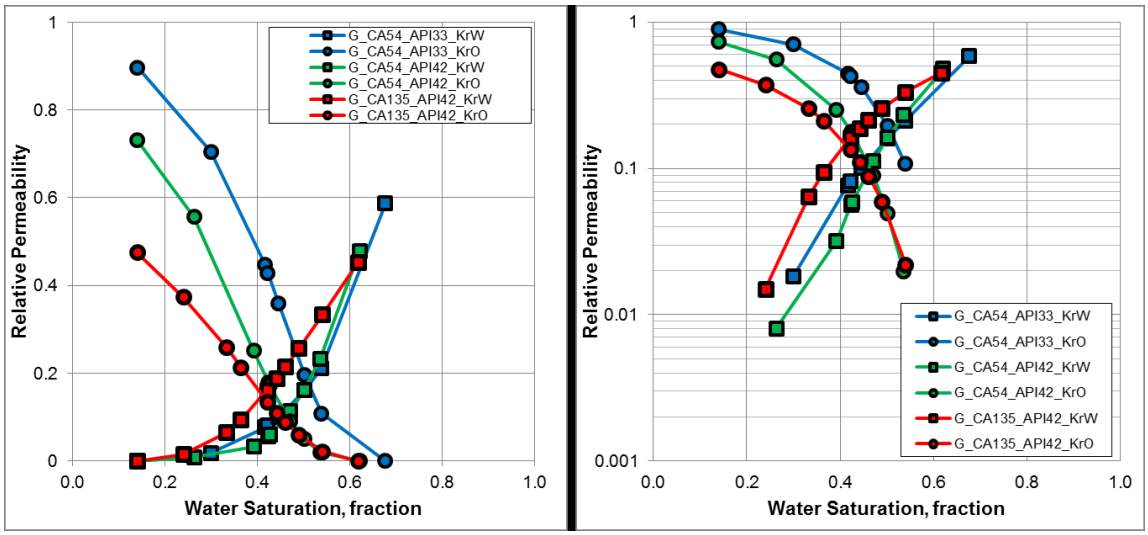

Figure 8: Relative permeability for sample G. Oil-wet case (red curves, contact angle 135^0, API 42), water-wet case 1 (blue curves, contact angle 54^0, API 33), and water-wet case 2 (green curves, contact angle 54^0, API 42).

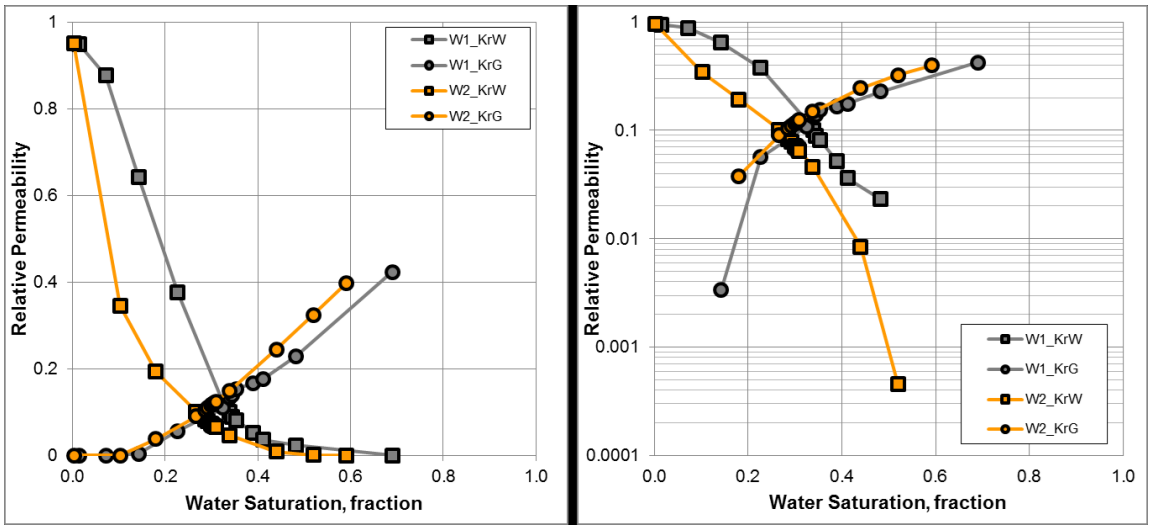

Figure 9: Relative permeability for two gas-water cases. The critical gas saturation for sample W1 is 0.14 and 0.18for sample W2.